

Article

The Mu2e Crystal Calorimeter: An Overview

Nikolay Atanov¹, Vladimir Baranov¹, Leo Borrel², Caterina Bloise³, Julian Budagov¹, Sergio Ceravolo³, Franco Cervelli⁴, Francesco Colao^{3,5}, Marco Cordelli³, Giovanni Corradi³, Yuri Davydov¹, Stefano Di Falco⁴, Eleonora Diociaiuti³, Simone Donati^{4,6}, Bertrand Echenard², Carlo Ferrari⁴, Antonio Gioiosa⁴, Simona Giovannella³, Valerio Giusti⁴, Vladimir Glagolev¹, Francesco Grancagnolo⁷, Dariush Hampai³, Fabio Happacher³, David Hitlin², Matteo Martini^{3,8}, Sophie Middleton², Stefano Miscetti^{3,*}, Luca Morescalchi⁴, Daniele Paesani³, Daniele Pasciuto^{4,6}, Elena Pedreschi⁴, Frank Porter², Fabrizio Raffaelli⁴, Alessandro Saputi⁹, Ivano Sarra³, Franco Spinella⁴, Alessandra Taffara⁴, Anna Maria Zanetti¹⁰ and Ren Yuan Zhu²

¹ Joint Institute for Nuclear Research, 141980 Dubna, Russia

² California Institute of Technology, Pasadena, CA 91125, USA

³ Laboratori Nazionali di Frascati dell'INFN, 00044 Frascati, Italy

⁴ INFN—Sezione di Pisa, 56100 Pisa, Italy

⁵ ENEA—Frascati, 00044 Frascati, Italy

⁶ Department of Physics, University of Pisa, 56100 Pisa, Italy

⁷ INFN—Sezione di Lecce, 73100 Lecce, Italy

⁸ Department of Engineering Sciences, Guglielmo Marconi University, 00193 Roma, Italy

⁹ INFN—Sezione di Ferrara, 44100 Ferrara, Italy

¹⁰ INFN—Sezione di Trieste, 34149 Trieste, Italy

* Correspondence: stefano.miscetti@lnf.infn.it



Citation: Atanov, N.; Baranov, V.; Borrel, L.; Bloise, C.; Budagov, J.; Ceravolo, S.; Cervelli, F.; Colao, F.; Cordelli, M.; Corradi, G.; et al. The Mu2e Crystal Calorimeter: An Overview. *Instruments* **2022**, *6*, 60. <https://doi.org/10.3390/instruments6040060>

Academic Editors: Fabrizio Salvatore, Alessandro Cerri, Antonella De Santo and Iacopo Vivarelli

Received: 5 September 2022

Accepted: 20 September 2022

Published: 9 October 2022

Publisher's Note: MDPI stays neutral with regard to jurisdictional claims in published maps and institutional affiliations.



Copyright: © 2022 by the authors. Licensee MDPI, Basel, Switzerland. This article is an open access article distributed under the terms and conditions of the Creative Commons Attribution (CC BY) license (<https://creativecommons.org/licenses/by/4.0/>).

Abstract: The Mu2e experiment at Fermilab will search for the standard model-forbidden, charged lepton flavour-violating conversion of a negative muon into an electron in the field of an aluminium nucleus. The distinctive signal signature is represented by a mono-energetic electron with an energy near the muon's rest mass. The experiment aims to improve the current single-event sensitivity by four orders of magnitude by means of a high-intensity pulsed muon beam and a high-precision tracking system. The electromagnetic calorimeter complements the tracker by providing high rejection power in muon to electron identification and a seed for track reconstruction while working in vacuum in presence of a 1 T axial magnetic field and in a harsh radiation environment. For 100 MeV electrons, the calorimeter should achieve: (a) a time resolution better than 0.5 ns, (b) an energy resolution <10%, and (c) a position resolution of 1 cm. The calorimeter design consists of two disks, each loaded with 674 undoped CsI crystals read out by two large-area arrays of UV-extended SiPMs and custom analogue and digital electronics. We describe here the status of construction for all calorimeter components and the performance measurements conducted on the large-sized prototype with electron beams and minimum ionizing particles at a cosmic ray test stand. A discussion of the calorimeter's engineering aspects and the on-going assembly is also reported.

Keywords: scintillation; crystals; SiPM; calorimetry

1. Introduction

The Mu2e experiment [1] at Fermilab aims to improve, by four orders of magnitude, the current single-event sensitivity in searching for the yet unobserved charged lepton flavour violating (CLFV) neutrino-less conversion of a negative muon into an electron in the field of an aluminium nucleus. Such a process, forbidden in the standard model, has a clear signature provided by the identification of a mono-energetic conversion electron (CE) with an energy slightly below the muon's rest mass (104.97 MeV). Even assuming neutrino oscillations, CLFV processes in the muon system remain completely negligible, $BR(\mu \rightarrow e \gamma) = 10^{-52}$ [2]. Observing CLFV candidates will indicate physics beyond the

standard model. If conversions are not observed, Mu2e will set a 90% upper limit on the ratio between the conversion and capture rates ($R_{\mu e}$) at $< 8 \times 10^{-17}$.

The Mu2e layout, based on an original concept by V. Lobashev and R. Djilibaev [3], is shown in Figure 1. The large solenoidal system is designed to largely increase the number of μ^- arriving at the stopping target (ST). A 8 GeV pulsed proton beam sent at the tungsten target inside the production solenoid (PS) produces low-momentum pions that are funnelled, by the graded field, inside the S-shaped transport solenoid (TS). Here, the pions decay to muons and are charge selected by a middle section collimator. At the end of the transport chain, a very intense negative muon beam ($\sim 10^{10}$ μ/s) enters the detector solenoid (DS) and is stopped at an aluminium target. In its lifetime, the experiment plans to collect 6×10^{17} muon stops to reach its sensitivity goal. Decay products are analysed by the tracker [4] and calorimeter [5] systems. Cosmic ray muons can produce fake CE candidates when interacting in the DS. To reduce their contribution, the external area of the DS and part of the TS are covered by a cosmic ray veto (CRV) [6] system.

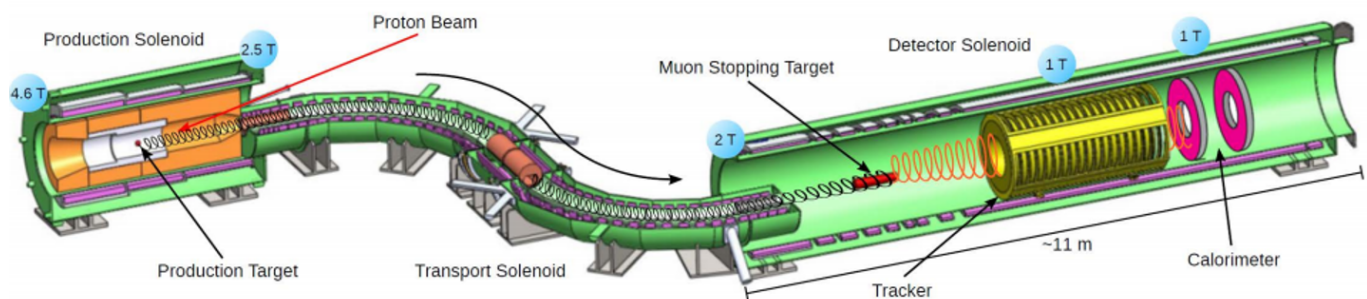


Figure 1. Layout of the Mu2e experiment: PS, DS, and TS solenoids are indicated in the picture. The cosmic ray veto, surrounding the DS and part of the TS solenoids, is not shown.

Muons stopped in the aluminium target form a muonic atom and cascade to the 1S ground state, with 39% decaying in orbit (DIO) and 61% captured by the nucleus. Low energy protons, neutrons, and photons are emitted in the nuclear capture process, thus originating both a large neutron fluence and, together with the flash of particles accompanying the beam, the bulk of the ionizing dose observed in the detectors. The tracker, composed of $\sim 20,000$ low-mass straw drift tubes, measures the charged particles' momenta by reconstructing their trajectories in the magnetic field with the detected hits. Full simulation shows that a momentum resolution of $O(160 \text{ keV})$ can be reached, thus separating the CE line from the fast-falling spectrum of the DIO electrons.

2. Materials and Methods

In this section, we describe the calorimeter system in more detail, starting from requirements and technical choices down to its engineering design.

2.1. Calorimeter Requirements

The calorimeter complements the CE identification tracker by providing a high μ/e rejection better than 200, a fast online trigger filter and a seed for track reconstruction [7]. To fulfil these tasks, simulation guided us to define the reconstruction requirements for 105 MeV electrons, which are summarized by this short list: (a) a large acceptance, (b) a time resolution better than 0.5 ns, (d) an energy resolution $< 10\%$, and (d) a position resolution of 1 cm. Moreover, the calorimeter should maintain its functionality when operating inside the DS without interruption for one year in a harsh radiation environment in the presence of 1 T axial magnetic field and in a region evacuated to 10^{-4} Torr. This asked for a high reliability, redundancy, and a high level of radiation hardness on all calorimeter components.

2.2. Technical Choices for Crystals and Photo-Sensors

Our solution was to design a high-quality crystal calorimeter with silicon photomultiplier (SiPMs) readout and a geometry organized into two annular disks (Figure 2) to maximize acceptance for spiralling electrons. The crystals had to provide a high light yield of at least 20 photoelectrons (p.e.)/MeV per single SiPM readout. To handle the pileup of particles, fast signals were needed, thus asking for crystals with a decay time (τ) better than 40 ns and front end electronics (FEE) providing fast amplified signals to be sampled at 200 Msps (5 ns binning) by the digitization system. The selected crystals, SiPMs had to sustain a total ionization dose up to 1000 Gy (900 Gy) and a neutron fluence of up to $3, 1.2 \times 10^{12}$ n/cm² respectively. All of this without deteriorating the calorimeter performance. The high redundancy and reliability required translated into having two independent SiPMs, FEE boards/crystal, and an independent digitization system for the two readout lines. A detailed simulation quantified that the typical mean time to failure (MTTF) needed to be $\sim 10^6$ h/component.

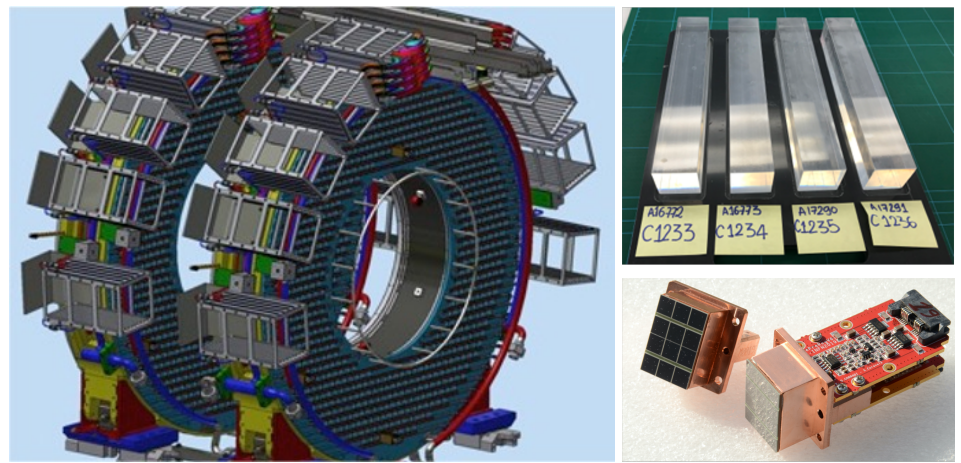


Figure 2. (Left), CAD of the two calorimeter disks. (Top right), few unwrapped calorimeter crystals with their own parallelepiped shape, and (bottom right), two SiPM arrays glued onto copper holder on the left and one readout unit formed by two SiPM arrays and two FEE boards mounted on its copper holder and on the right.

At the end of the R&D program [8–10], undoped CsI crystals were chosen as the best compromise between cost, performance, and reliability, being sufficiently radiation hard for our task and having a fast emission time and an acceptable light yield. Since the main scintillation component has a wavelength of 310 nm to well match the SiPM photon detection efficiency (PDE) as a function of wavelength, we selected Hamamatsu UV extended SiPMs, where the front window epoxy was replaced by a silicon resin to achieve $>20\%$ PDE down to 280 nm. To operate in a vacuum and minimize outgassing contributions, the crystal SiPM coupling was performed without any optical grease. This choice reduced the light collected by the SiPM, so we opted to build a very large area (12×16 mm²) SiPM array. In Figure 2 (bottom right), a picture of two Mu2e SiPMs glued to a copper holder is shown, each one consisting of the parallel of two series of three 6×6 mm² monolithic Hamamatsu surface mount SiPMs, model S13360-6050PE, with 50 μ m pixel size. This configuration reduced the array capacitance and quenching time while simplifying the FEE design.

2.3. Electronics Scheme

The electronics is based on analogue FEE cards directly connected to the SiPM pins and a digital readout part distributed on the crates surrounding the disk.

The FEE shapes and amplifies the signal while locally regulating the supplied voltage. The two SiPMs glued to a copper holder, assembled together with two FEE boards and a copper Faraday cage, constitute a readout unit (ROU).

The digital boards are subdivided in a mezzanine (MB) for controlling the HV and monitor the current and temperature of SiPMs and a readout and digitization board (DIRAC) that performs the zero suppression and samples the signals with 5 ns binning. Each digital board is able to handle 20 channels. Much effort was dedicated to design and produce boards that work well in a magnetic field and in the radiation-harsh Mu2e environment. A description of all the details of the electronics scheme, the radiation hardness program, and the quality tests performed can be found elsewhere [11,12].

2.4. Breakdown of Mechanical Layout

Figure 3 shows a breakdown of the calorimeter structure.

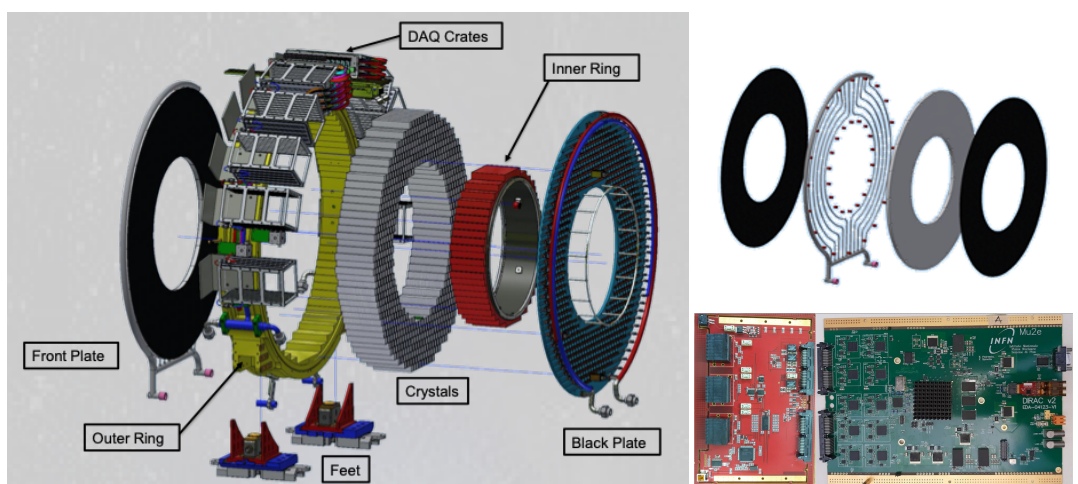


Figure 3. (Left) breakout of calorimeter mechanical components; (top right), breakdown of front panel plate embedding source tubing; and (bottom right), the mezzanine and DIRAC boards.

Each disk is filled with a matrix of 674 parallelepiped undoped CsI crystals ($34 \times 34 \times 200 \text{ mm}^3$) for an inner/outer diameter of 650 mm/1314 mm. The crystals are wrapped in $150 \mu\text{m}$ thick Tyvek foils and separated from each other with $50 \mu\text{m}$ thick Tedlar foil to make the optical cross talk negligible. The crystal matrix is supported externally by an aluminium shaped outer ring, with an outer diameter of 1460 mm and a thickness of 146 mm to provide the required stiffness. The disk is milled to shape to form the lateral steps where crystal rows are positioned and aligned. The outer ring also provides support and the place where all other components are fastened. It hosts the custom DAQ crates in its external surface and their cooling manifold.

In order to minimize the energy loss of particles arriving to the crystals, the inner ring and the front plate, which are traversed by particles, are made in carbon fibre with embedded light aluminium honeycomb structures, thus achieving the right stiffness while avoiding vacuum virtual leaks. The inner ring occupies the inner bore surface, sustains the crystal vertical load, and grants a reference for the positioning of the crystal matrix. The front plate is the frontal protection cover of the crystal matrix and hosts 10 thin-wall aluminium tubes, symmetrically arranged on each disk, to flow the calibration source fluid (FC-770).

Finally, in the back of the crystals, the back plate constitutes the rear mechanical enclosure of the calorimeter disk. The back plate is created from a 20 mm thick PEEK plate milled to shape to host and support the 674 ROUs. PEEK has been chosen for its good outgassing characteristics and to optimize the thermal isolation of the electronics. The FEE plate embeds a network of 38 parallel vacuum brazed copper lines, where a cooling liquid (3M NOVEC HFE 1700) will be circulated at $-15 \text{ }^\circ\text{C}$ to cool down the SiPMs in

the ROUs. The latter ones will be fastened on the cooling lines to optimize the thermal conductivity. The stainless steel manifolds, placed on the outer plate border, distribute the cooling fluid to the copper lines. More details on the mechanical components can be found elsewhere [13].

2.5. Calibration Systems

The crystal-by-crystal energy equalization is obtained by means of a calibration system, formerly devised for the BaBar calorimeter [14], where a 6.13 MeV photon line is obtained from a short-lived ^{16}O transition. The decay chain comes from a FluorinertTM coolant liquid (FC-770) that is activated by fast neutrons produced by a DT generator. The activated liquid circulates in the aluminium tubes positioned in the front plate to uniformly illuminate each crystal face. The source system is accompanied by a laser monitoring system that provides a continuous monitoring of the sensor gains and of each channel timing offsets. Each crystal is illuminated by the laser light coming from the laser head via primary and secondary distribution systems, through an optical fibre whose needle is inserted in the ROU structure. The laser offers also a simple method to monitor variations in the energy and timing resolutions. Usage of cosmic ray and DIO events is foreseen for a continuous in situ energy and timing calibration during operation.

3. Results

3.1. Calorimeter Qualification with Module-0

Before starting production, a large size prototype, dubbed Module-0, was assembled to mimic the calorimeter disk and confirm technical choices, drive the readout electronics development, and test its performance. The prototype, assembled in May 2017 with 51 crystals and 102 SiPMs, was equipped with the first FEE version and tested with an electron beam at BTF (Frascati) soon after its assembly. The digital readout was based on commercial CAEN digitizers. A detailed description of the test beam can be found elsewhere [15]. The main results are summarized by an energy and timing resolution parametrized as the quadrature of stochastic $a/\sqrt{(E/\text{GeV})}$, noise, $b/(E/\text{GeV})$, and constant, c , terms, as in Table 1. The main conclusion for the energy was that the stochastic term was consistent with a light yield of $O(20 \text{ pe/MeV/SiPM})$, the noise term was attributed to an electronic noise of $O(400) \text{ keV/channel}$, and a coherent noise related to the used digitizers, while the c term, the dominant one, was due to shower leakage effects, as demonstrated by a Geant4 simulation. The runs at 0° had energy loss due to longitudinal leakage. The runs at 50° exacerbated the b and c terms due to longer clusters and higher transversal leakage. Overall, a resolution better than 5 (7.5)% was achieved at 100 MeV for runs at normal (50°) incidence. The timing resolution, determined by time difference between the two SiPMs/crystals, showed a constant term of 91 (118) ps and a noise term of 6.8 (8.9) ps/E/GeV at normal (at 50°) incidence, granting a timing resolution better than 200 ps at 100 MeV. These results fully satisfied the calorimeter requirements and provided a green light for the production of components. In the last five years, we have used Module-0 also to study the behaviour in a vacuum, at low temperature, and for carrying out vertical slice tests of increasing complexity at a cosmic ray test stand. In Figure 4 (left), a picture of Module-0 inside the vacuum vessel can be seen. In Figure 4 (right), the distribution of the time difference between all pairs of crystals, with energy deposition consistent with an MIP, is shown before and after the T_0 calibration procedure. A clear gaussian peak is observed, consistent with a mean time resolution of 300 ps for a 20 MeV energy deposition. Time improvements depend on the fit procedure of the pulse shape and are presented elsewhere [12].

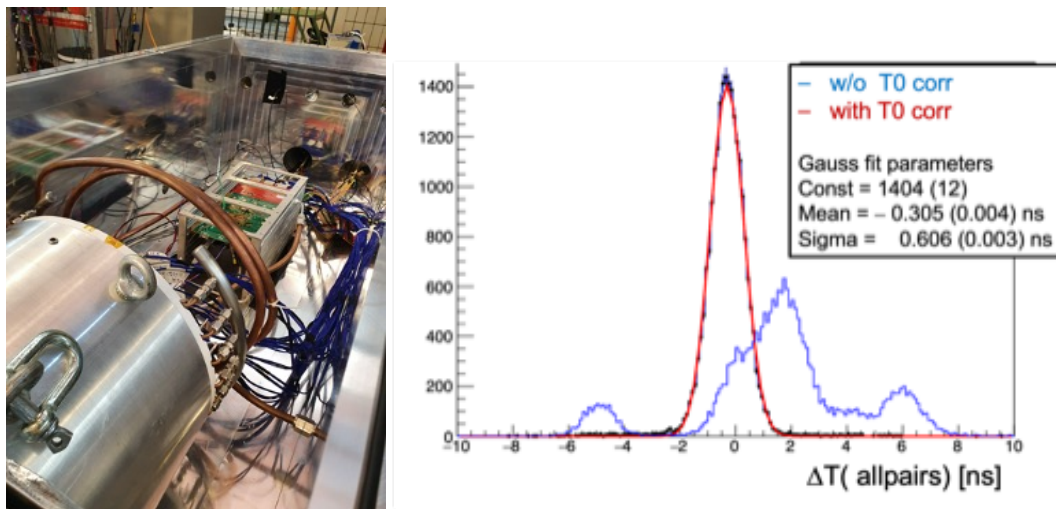


Figure 4. Operations with Module-0: (left), picture of Module-0 inside the vacuum vessel readout with MB and DIRAC boards; (right), distribution of time differences between all crystal pairs, before (blue) and after (red) T0's calibration.

Table 1. Parametrization of energy and time resolution for Module-0 electron test beam. The numbers in parentheses represent one sigma uncertainties.

Params	$\frac{\sigma_E}{E}$ (%) at 0°	$\frac{\sigma_E}{E}$ (%) at 50°	σ_t (ps) at 0°	σ_t (ps) at 50°
a	0.6	0.6	-	-
b	0.27 (0.03)	0.37 (0.04)	6.8 (0.1)	8.9 (0.2)
c	4.05 (0.27)	5.86 (0.39)	91 (4)	118 (7)

3.2. Production of Crystals, SiPMs and FEE

The production of basic components started in 2018. We successfully completed procurement and quality testing of 4000 SiPMs in 2019, 1500 crystals in 2020, and 3300 FEE boards in 2021. The electronics production was delayed by the pandemic and by the need to make new electronics releases for improving its radiation hardness, as reported elsewhere [12].

The crystals were produced by SICCAS (China) and St.Gobain (France), while the SiPMs were produced by Hamamatsu (Japan). The quality of crystal and SiPM production was excellent, as shown by the reference pictures in Figure 5 (left,center). The optical parameters of the production crystals from both producers were acceptable [16], while St.Gobain's crystals evidenced some difficulties in matching the 100 μm precision of the mechanical realization of the parts. In the end, 8% of the crystals were replaced by relying only on SICCAS for a new production of the final batches. The SiPM performed as expected with a very high quality [17,18] on gain, PDE, and dark current values and a rejection factor smaller than 2%.

The FEE was produced by ARTEL (Italy) with a negligible rejection factor, albeit all boards underwent a burn-in test at 65 °C in a climatic chamber in JINR (Dubna, Ru), followed by a calibration phase for both HV, gain, and differential linearity parameters (see Figure 5 (right)). At the moment of writing, we have reacquired 2500 FEE units from JINR after burn-in and calibration.

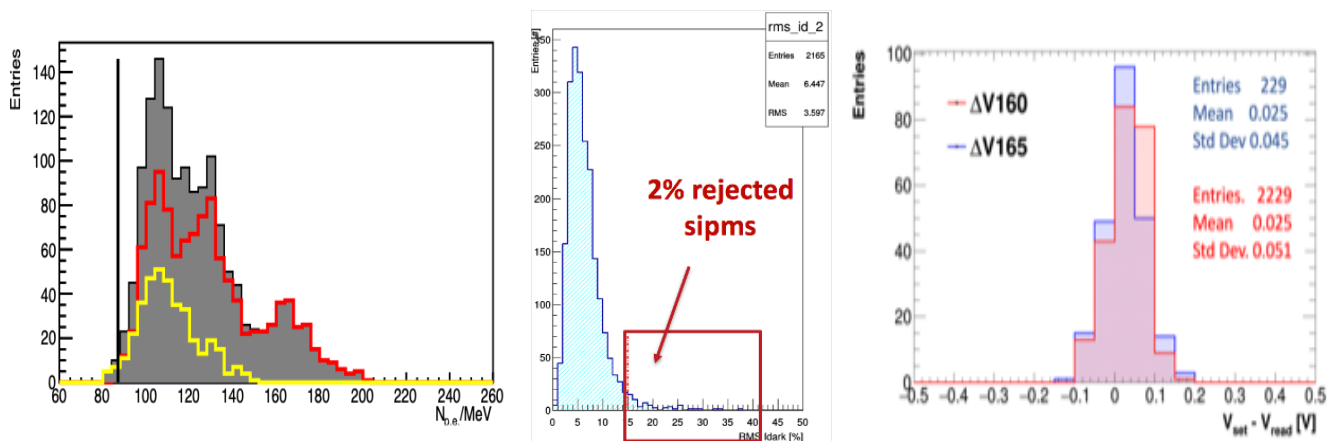


Figure 5. Crystals, SiPMs, and FEE production: **(left)**, light yield of crystals (Npe/MeV) as obtained with a large-area PMT fully covering the crystal readout face, the red (yellow) distribution is for the SICCAS (St.Gobain) production crystals; **(center)**, RMS of Idark (%) of each SiPM array; **(right)**, precision of HV settings for the FEE boards.

3.3. Preparation and Test of the Readout Units

The preparation and test of the readout units (ROUs) is advanced. Two Mu2e SiPMs were glued to each copper holder, as shown in Figure 2 (bottom right), by relying on the EP30AN MasterBond thermal glue with a good performance in vacuum. In total, 3000 production SiPMs were glued to 1500 SiPM holders with a precise glue distribution machine developed at INFN Frascati (LNF). After this operation, we started assembling the calibrated FEE. So far, we have assembled 70% of the entire production lot.

In the last year, we have also dedicated a lot of effort to design, realize, and put into operation a semi-automated quality station to calibrate the ROUs. In a 10 min run, the gain, PDE, and charge response in a $(-4:+2)$ V region around the operational voltage, V_{op} , were evaluated. Currently, we have performed a quality test for 600 ROUs, achieving a gain reproducibility better than 2%, with a channel-by-channel gain spread at a level of 3–4% along production. A much more detailed explanation of the station functionality and its results can be found elsewhere [12,19].

3.4. Production and Assembly of the Calorimeter Mechanical Structure

In the last two years, all large mechanical parts were produced by Italian firms, as shown in Figure 6. The first pieces realized were the two outer rings, produced by Cerasa Mechanics (Assisi). They were milled by a single aluminium block providing the right stiffness and excellent precision on the final step edges. The back plate was built in PEEK by CINEL (Vigonza). Its picture, shown in Figure 6 (top right), was taken during the leak test of the cooling lines with a helium sniffer. The measured leak rate was below 10^{-10} atm \times cc/s. A test of temperature uniformity of the same lines was carried out in INFN Pisa laboratories by flowing HFE at 50 °C and controlling with a thermal camera. The parts with composed materials were built by CETMA (Brindisi). On Figure 6 (bottom-left), a picture of the inner ring can be seen, soon after being completed. Once at LNF, a series of stiffness tests were performed loading this structure vertically with more than 100 kg. Deformations observed were below 400 μ m as expected. In Figure 6 (bottom-right), the front plate is shown. This plate was completed integrating the source aluminium tubing in grooves on the internal aluminium honeycomb. The source tubing was realized by Caltech and Fermilab.



Figure 6. Calorimeter mechanical parts: (top left), outer ring; (top right), FEE plate; (bottom left), inner ring; (bottom right), front plate with source tubing embedded in the aluminium honeycomb.

Before shipping all mechanical parts to Fermilab, a dry fit was carried out in a clean room at LNF to check that all pieces were well fitting. In this occasion, we also assembled, on the external outer ring surface, the ten crates produced by TecnoAlarm (Rome) and their cooling manifolds (Figure 7 (left)). A careful vacuum leak test was performed on both the crate manifolds and the elbow joints between the crates and manifolds. Only two small leaks were detected in two of the lowest elbows and fixed locally by Tig welding. At the end of this operation, a maximum leak rate of 10^{-10} atm \times cc/s was achieved, satisfying the experiment's requirements. Other components, such as the feet, the disk support stands, and other smaller mechanical parts, have been built by Italian firms and completed with the support of the LNF mechanical shops.

In June 2022, we started the final assembly of the downstream disk in a ISO-7-class clean room located at SIDET, Fermilab. The operation sequence started with mounting and aligning the outer ring over its stand, and progressed with alignment of the inner ring. As soon as this was completed and the survey indicated a reproducible and stable detector assembly, we started stacking crystals.

The stacking proceeded from the bottom to top for increasing rows, following an optimized crystal placement obtained by examining the whole crystal production parameters and positioning: (i) the ones with higher (lower) light yield, faster (slower) signals, and reduced (increased) radiation-induced currents in the innermost (outermost) rings where more (less) radiation dose is expected and (ii) the remaining ones in the central regions. While selecting the crystals/rows we also minimized the flatness of the row thickness. Before stacking the crystals on the outer disk, a set of two-day-long outgassing runs were performed in a dedicated vacuum vessel to reduce the single-crystal outgassing level to below 10^{-7} Torr \times l/s. Between each stacked row, an additional 50 μ m Tedlar layer was placed. To keep the crystal matrix solidly connected, each row was compressed using screws pushing on plastic shims at both row ends. The accuracy of crystal stacking was checked while operating using a high-precision bubble level and then confirmed offline with a laser tracker. The crystal stacking proceeded steadily, having previously completed the outgassing operation, so that in less than a month (see Figure 7 (right)), the downstream disk had all of the crystal matrix inserted.

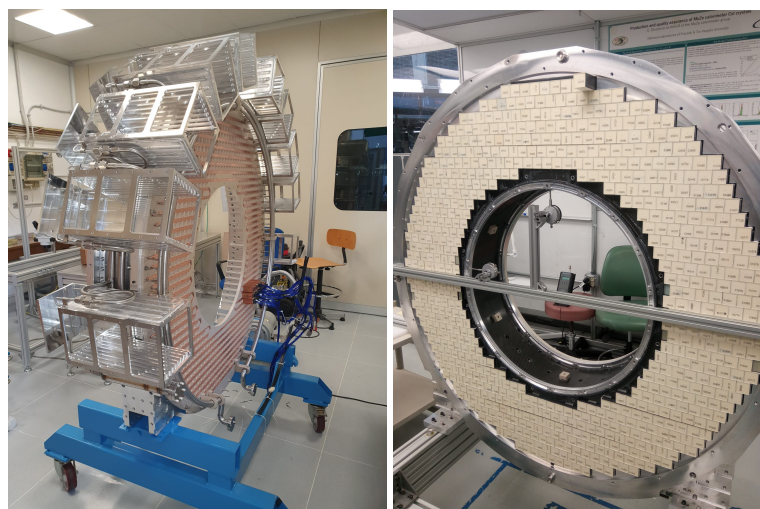


Figure 7. Current status of calorimeter assembly: **(left)**, a dry fit of the upstream disk mechanical structure in the LNF clean room; **(right)**, the downstream disk with all 674 crystals inserted at Fermilab SIDET clean room.

4. Discussion

The Mu2e calorimeter demonstrated that its requirements are satisfied through the tests carried out with Module-0 (see Section 3.1). However, it could face some difficulties in maintaining the required resolutions, while operating in a vacuum, and in a radiation-harsh environment. We solved these problems by combining a mix of technical choices to a high level of engineering. The crystals, SiPMs, and FEE have proven to be radiation hard up to the maximum level of TID and neutron fluence expected at the end of the experimental lifetime [12]. The most relevant effect we will observe while running will be the rapid increase in SiPM leakage current (I_{dark}) under neutron irradiation, requiring us to cool down the SiPMs to $-10\text{ }^{\circ}\text{C}$ to maintain operation. To control the correctness of our choices, we carried out two dedicated measurements:

(1) Measurement of the I_{dark} increase as a function of the neutron fluence. For each SiPM production batch, we randomly chose five units for irradiation purposes. While the TID test indicated no relevant increase in I_{dark} , irradiation with neutrons showed otherwise. Two neutron irradiation facilities, one at EPOS (HZDR, Dresden) and one at Enea-FNG (Frascati), were used. The two measurements indicated, for the same irradiation level, a $O(1.5)$ difference in the increase in I_{dark} . While data are still being analysed, we conservatively used the case with the largest I_{dark} increase, looking at several SiPMs exposed at different fluences at FNG. A first summary result is reported in Figure 8 (left), where the average I_{dark} is shown as a function of temperature at different overvoltages ($\Delta V = V - V_{\text{brk}}$) for two different fluences. Please note that the supplied bias is three times larger than the one of a monolithic Hamamatsu SiPMs due to the series configuration. These data confirm that decreasing the temperature by $10\text{ }^{\circ}\text{C}$ corresponds to a decrease in I_{dark} by a factor of two, and that this current is linearly proportional to the fluence. The bottom plot guides the running condition in the experiment. We expect to operate the SiPMs at $-10\text{ }^{\circ}\text{C}$ to keep the leakage current inside our maximum operation limit of 2 mA/SiPM , with a minor bias adjustment.

(2) Measurement of the time resolution achieved with irradiated sensors. The second measurement tested the effect of neutron irradiated sensors on the resolution. For our benchmark, we used sensors exposed to a fluence of $5 \times 10^{11}\text{ n/cm}^2$ and kept at $0\text{ }^{\circ}\text{C}$, that are equivalent to the sensors exposed to the fluence expected at experiment lifetime $1.2 \times 10^{12}\text{ n/cm}^2$, if kept at $-10\text{ }^{\circ}\text{C}$. While for the energy, we estimated that 2 mA current corresponds to a noise level of $O(1.5\text{ MeV})$ to be added independently to each fired channel, it was more difficult to evaluate the effect on time resolution, since a fit to the waveform signals was needed. A systematic test was carried out with a 50 picosecond Hamamatsu

laser illuminating crystals readout with one irradiated and one non-irradiated SiPM. The resolution obtained as a function of the reconstructed charge is shown in Figure 8 (right). To provide an indication of the energy scale, 2500 pC corresponded to 1 MiP energy deposition, i.e., 20 MeV. The result of 700 ps timing resolution achieved with one SiPM at a fluence of $5 \times 10^{11} \text{ n}_{1\text{MeVeq}}/\text{cm}^2$, and the nice trend with energy, demonstrated that even with only one irradiated sensor, we can reach a resolution better than 500 ps for a 100 MeV energy deposition.

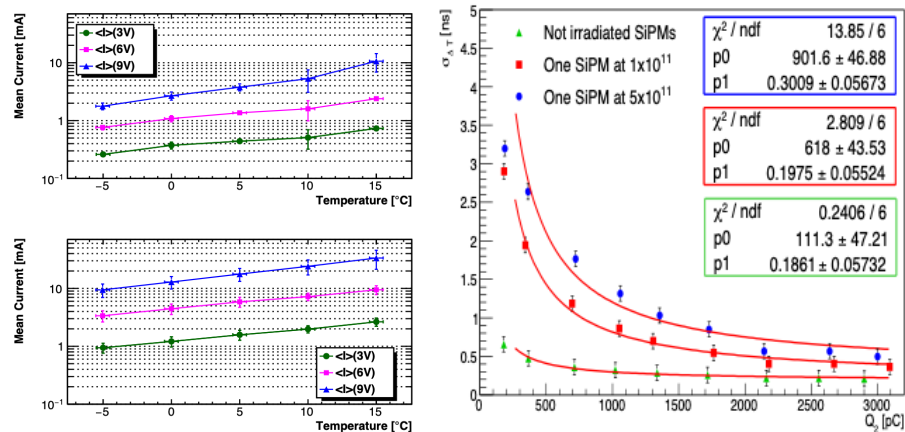


Figure 8. (Left) Idark dependence on SiPM temperature for different levels of neutron fluence (top, 10^{11} , bottom $5 \times 10^{11} \text{ n}_{1\text{MeVeq}}/\text{cm}^2$) and overvoltages. (Right), time resolution dependence on charge for SiPM irradiated at different neutron fluences and running at 0 °C.

5. Conclusions

In this paper, we summarized the construction status of the Mu2e calorimeter that will complement the tracking and CRV systems in identifying conversion electrons.

The chosen undoped CsI crystals proved to have fast signals and a large light yield when readout with our custom design UV-extended SiPMs. The production of 1500 crystals and 4000 Mu2e SiPM was successfully completed before the pandemic started, satisfying all required production parameters. In the last two years, we have also completed the development and production of 3300 radiation-hard FEE boards as well as the production of all mechanical components. A lot of effort has been dedicated to the assembly and test of the ROUs, which is more than halfway completed. All the mechanical components have been successfully first assembled in a dry fit at LNF and then at Fermilab for the crystal stacking operation. The crystal stacking of the first disk has been completed at the moment of writing. We are now waiting the shipment from INFN to Fermilab of the front plate in composite material, where the source aluminium tubes have also been integrated. The front plate will conclude the assembly of the mechanical parts.

Meanwhile, the production of the digital electronics is under way. Due to the pandemic, there are a lot of delays to the FPGA delivery time, so we will start cabling the detector from the FEE to the mezzanine boards in the fall of this year and postpone the integration of the digital readout boards (DIRAC) to the spring of 2023. In parallel, we plan to start the construction of the second disk this fall. Finally, we foresee the performance of an integrated test of calorimeter readout in summer 2023, before preparing for installation on the detector rails. In parallel, we will complete the infrastructure for the calibration systems and for the cooling station, needed for operation in Mu2e, looking forward to a successful experiment in the following years.

Author Contributions: Conceptualization, writing, project administration: S.M. (Stefano Miscetti); the rest of the work was really done as a common work with all other authors. All authors have read and agreed to the published version of the manuscript.

Funding: This research was funded and supported by all institutions listed on the acknowledgments section.

Data Availability Statement: Not applicable.

Acknowledgments: We are grateful for the vital contributions of the Fermilab staff and the technical staff of the participating institutions. This work was supported by the US Department of Energy; the Istituto Nazionale di Fisica Nucleare, Italy; the Science and Technology Facilities Council, UK; the Ministry of Education and Science, Russian Federation; the National Science Foundation, USA; the Thousand Talents Plan, China; the Helmholtz Association, Germany; and the EU Horizon 2020 Research and Innovation Program under Marie Skłodowska-Curie Grant Agreement Nos. 101003460, 101006726, 734303, 822185, and 858199. This document was prepared by members of the Mu2e Collaboration using the resources of the Fermi National Accelerator Laboratory (Fermilab), U.S. Department of Energy, Office of Science, HEP User Facility. Fermilab is managed by Fermi Research Alliance, LLC (FRA), acting under Contract No. DE-AC02-07CH11359.

Conflicts of Interest: The authors declare no conflict of interest.

References

1. Bartoszek, L.; Barnes, E.; Miller, J.P.; Mott, J.; Palladino, A.; Quirk, J.; Roberts, B.L.; Crnkovic, J.; Polychronakos, V.; Tishchenko, V.; et al. The Mu2e Collaboration. Mu2e technical design report. *arXiv* **2015**, arXiv:1501.05241.
2. Bilenky, S.M.; Petcov, S.T.; Pontecorvo, B. Lepton mixing, $\mu \rightarrow e\gamma$ decay and neutrino oscillations. *Phys. Lett. B* **1977**, *67*, 309–312. [[CrossRef](#)]
3. Lobashev, V.; Djilibaev, R. On the search for $\mu \rightarrow e$ conversion on Nuclei. *Sov. J. Nucl. Phys.* **1989**, *49*, 384–385.
4. Lee, M.J. Mu2e Collaboration. The straw tube tracker for the Mu2e experiment. *Nucl. Phys. B Proc. Suppl.* **2016**, *273–275*, 2530–2532.
5. Atanov, N.; Baranov, V.; Bloise, C.; Budagov, J.; Cervelli, F.; Ceravolo, S.; Colao, F.; Cordelli, M.; Corradi, G.; Davydov, Y.I.; et al. Design and status of the Mu2e calorimeter. *IEEE Trans. Nucl. Sci.* **2018**, *65*, 2073–2080. [[CrossRef](#)]
6. Artikov, A.; Baranov, V.; Blazey, G.C.; Chen, N.; Chokheli, D.; Davydov, Y.; Dukes, E.C.; Dyckant, A.; Ehrlich, R.; Francis, K.; et al. Photoelectron Yield of scintillating counters with embedded wavelength shifting fibers read out with silicon photomultipliers. *Nucl. Instrum. Meth. A* **2018**, *890*, 84–95. [[CrossRef](#)]
7. Atanov, N.; Baranov, V.; Budagov, J.; Ceravolo, S.; Cervelli, F.; Colao, F.; Cordelli, M.; Corradi, G.; Dane, E.; Davydov, Y.; et al. The Mu2e calorimeter final design report. *arXiv* **2018**, arXiv:1802.06341.
8. Atanov, N.; Baranov, V.; Colao, F.; Cordelli, M.; Corradi, G.; Dane, E.; Davydov, Y.I.; Flood, K.; Giovannella, S.; Glagolev, V.; et al. Measurement of time resolution of the Mu2e LYSO calorimeter prototype. *Nucl. Instrum. Meth. A* **2016**, *812*, 104–111. [[CrossRef](#)]
9. Atanov, N.; Baranov, V.; Colao, F.; Cordelli, M.; Corradi, G.; Dane, E.; Davydov, Y.I.; Flood, K.; Giovannella, S.; Glagolev, V.; et al. Energy and time resolution of a LYSO matrix prototype for the Mu2e experiment. *Nucl. Instrum. Meth. A* **2016**, *824*, 684–685. [[CrossRef](#)]
10. Atanov, N.; Baranov, V.; Budagov, J.; Carosi, R.; Cervelli, F.; Colao, F.; Cordelli, M.; Corradi, G.; Dane, E.; Davydov, Y.I.; et al. Design and status of the Mu2e electromagnetic calorimeter. *Nucl. Instrum. Meth. A* **2016**, *824*, 695–698. [[CrossRef](#)]
11. Ceravolo, S.; Colao, F.; Diociaiuti, E.; Corradi, G.; Di Falco, S.; Donati, S.; Fiore, S.; Ferrari, A.; Gioiosa, A. Design and qualification of the Mu2e electromagnetic calorimeter electronics system. In Proceedings of the 15th Pisa Meeting on Advanced Detectors, Isola d’Elba, Livorno, Italy, 22–27 May 2022.
12. Atanov, N.; Baranov, V.; Borrel, L.; Bloise, C.; Budagov, J.; Ceravolo, S.; Cervelli, F.; Colao, F.; Cordelli, M.; Corradi, G.; et al. Mu2e crystal calorimetry front-end electronics: Design and characterization. In Proceedings of the Special Issue of Instruments 2022 Selected Papers from the 19th International Conference on Calorimetry in Particle Physics (Calor 2022), Brighton, UK, 16–20 May 2022.
13. Atanov, N.; Baranov, V.; Borrel, L.; Bloise, C.; Budagov, J.; Ceravolo, S.; Cervelli, F.; Colao, F.; Cordelli, M.; Corradi, G.; et al. Development, construction and test of the Mu2e electromagnetic calorimeter mechanical structures. *JINST* **2022**, *17*, C01007. [[CrossRef](#)]
14. Aubert, B.; Bazan, A.; Boucham, A.; Boutigny, D.; De Bonis, I.; Favier, J.; Gaillard, J.-M.; Jeremie, A.; Karyotakis, Y.; Le Flour, T.; et al. The BABAR detector. *Nucl. Instrum. Meth. A* **2002**, *479*, 1–116. [[CrossRef](#)]
15. Atanov, N.; Baranov, V.; Budagov, J.; Caiulo, D.; Cervelli, F.; Colao, F.; Cordelli, M.; Davydov, Y.I.; Di Falco, S.; Diociaiuti, E.; et al. Design and test of the Mu2e un-doped CsI + SiPM crystal calorimeter. *Nucl. Instrum. Meth. A* **2019**, *936*, 94–97. [[CrossRef](#)]
16. Atanov, N.; Baranov, V.; Budagov, J.; Davydov, Y.I.; Glagolev, V.; Tereshchenko, V.; Usubov, Z.; Cervelli, F.; Di Falco, S.; Donati, S.; et al. Quality assurance on un-doped CsI crystals for the Mu2e experiment. In Proceedings of the 2017 IEEE Nuclear Science Symposium and Medical Imaging Conference (NSS/MIC), Atlanta, GA, USA, 21–28 October 2017; pp. 752–757.
17. Cordelli, M.; Cervelli, F.; Diociaiuti, E.; Donati, S.; Donghia, R.; Di Falco, S.; Ferrari, A.; Giovannella, S.; Happacher, F.; Martini, M.; et al. Pre-production and quality assurance of the Mu2e calorimeter Silicon Photomultipliers. *Nucl. Instrum. Meth. A* **2018**, *912*, 347–349. [[CrossRef](#)]

18. Atanov, N.; Baranov, V.; Budagov, J.; Caiulo, D.; Cervelli, F.; Colao, F.; Cordelli, M.; Corradi, G.; Davydov, Y.I.; Di Falco, S.; et al. The Mu2e calorimeter: Quality assurance of production crystals and SiPMs. *Nucl. Instrum. Meth. A* **2019**, *936*, 154–155. [[CrossRef](#)]
19. Sanzani, E.; Bloise, C.; Ceravolo, S.; Cervelli, F.; Colao, F.; Cordelli, M.; Corradi, G.; Falco, S.D.; Diociaiuti, E. An automated QC station for the calibration of the Mu2e calorimeter Readout Units. In Proceedings of the 1th Pisa Meeting on Advanced Detectors, Isola d'Elba, Livorno, Italy, 22–27 May 2022.